Time-of-flight Measurements at HILITE

Bachelor thesis

at the GSI Helmholtzzentrum für Schwerionenforschung GmbH
on behalf of the Goethe Universität Frankfurt

provided by
Béla Arndt

Frankfurt, December 2018

Thesis in the summer:

Es ist sehr heiß,
die Bahn ist voll.
Es stinkt nach Schweiß,
ich hege Groll

Die Bahn braucht lang,
die Zeit verinnt.
Kein Sturm, kein Drang,
das Warten beginnt.

Ich komme nicht an,
mein Chef ist sauer.
Jetzt bin ich dran,
er haut mich... Aua[1]

Bela Arndt 2018

---

[1]No Bachelor studends where harmed during the making of this thesis.

Contents

1 Introduction

The preparation of ions in Penning traps has led to a number of important scientific discoveries during the last 50 years. Besides the prominent g-factor measurements of H.G. Dehmelt in 1959 and 1961 [1], many other experiments have profited from the cooling and confinement advantages that Penning traps provide. Long storage times, charge/mass separation, good localisation and density manipulation are just some of the assets of Penning traps making them the right candidate for HILITE (High intensity Laser ion trap experiment).[2]

The HILITE-Experiment aims for a better understanding of quantum electrodynamics in high intensity laser fields. "Laser systems capable of producing high intensities also at photon energies in the extreme ultra-violet (EUV) and (soft) X-ray regime open access to novel effects like nonlinear Compton effects or simultaneous elastic and inelastic photon scattering, and allow multiphoton-ionisation experiments in a new domain." [3] Crucial for the observation of these effects is good target preparation, manipulation and a reliable way of measuring the reaction products.

To provide suitable targets for HILITE a portable Penning trap has been constructed and is currently tested at the GSI facility in Darmstadt. The reasons for a portable device are a planed experiments at the JETI Laser system located in the Helmholtz Institute for Optical Physics in Jena [4], as well as the possibility to visit other research centers in the future. A side effect of the added mobility is the need for a self-sustained ion source which was solved using an Electron Beam Ion Trap (EBIT)[5].

The main focus of this bachelor thesis is the characterisation of the ions provided by this EBIT with respect to different charge states, extraction settings and a residual gas measurement. Since the ion capture process in the Penning trap is dependent on efficient deceleration as well as precise timing, there is a need for an investigation of the flight time between the ions source and the trap. As a part of this thesis the influence of different parts of the experimental setup on this time-of-flight has been measured.

2 Theoretical Motivation

2.1 Ion Motion in Electric and Magnetic Fields

Since an important part of this thesis are time-of-flight measurements with variable electric and magnetic fields, a short introduction to the theoretical background is useful.

Two of the main applications of electric fields at the HILITE experiment are the acceleration and the deceleration of ions. For a better understanding this process one can connect the potential energy E_{pot} of a given ion to the electric potential U_{e}

$$E_{\text{pot}} = U_{\text{e}} \cdot q. \tag{2.1}$$

with q being the charge of the ion in electron volt. By leaving this potential to an area of zero electric potential the energy gets converted into kinetic energy. This leads to an expression connecting the velocity v and the electric potential U_e:

$$v = \sqrt{\frac{2U_e q}{m}}, \tag{2.2}$$

It is well known and understood that the force acting on charged particles in a magnetic field is the Lorentz force. With q being the charge, $\vec{v}$ the speed and $\vec{B}$ the applied magnetic field, one can describe the Lorentz force on a particle

$$\vec{F}_{\text{L}} = q(\vec{v} \times \vec{B}). \ [6] \tag{2.3}$$

By evaluation of the cross product in Equation 2.3 one can conclude that the velocity and the Lorentz force are perpendicular to each other, resulting in a circular motion. The frequency and radius of the cyclotron motion can be written as:

$$r = \frac{mv_\perp}{qB}; \tag{2.4}$$

$$\omega_{\text{c}} = \frac{qB}{m}. \tag{2.5}$$

The next step is to investigate the behavior of charged particles in inhomogeneous fields. Using energy conservation and the fact that the magnetic field does no work ($\nabla \vec{B} = 0$) on particles one can derive this important identity

$$v_\perp^2 + v_\parallel^2 = const.. \tag{2.6}$$

Together with the definition of the magnetic moment μ as the radial current I including a plane A, one finds that the identity above can be rewritten as:

$$\mu = I \cdot A = \frac{mv_\perp^2}{2B} \implies \frac{1}{2}mv_\parallel^2 + f\mu B = const., \tag{2.7}$$

with f being the correction factor for μ, because μ is an adiabatic constant. Closer investigations show that μ is only constant if the following condition applies:

$$\frac{2\pi}{\omega_c} \cdot \left| \frac{\delta B}{\delta t} \right| >> B. \ [7] \tag{2.8}$$

2.2 Penning Traps

As the manipulation of particles in a Penning trap is one of the key assets of HILITE, a brief introduction to Penning traps can be of use. A Penning trap is a device used for the confinement of charged particles. It uses a combination of a magnetic and an electric field to achieve 3-dimensional confinement. The ideal Penning trap consists of a magnet creating a homogeneous magnetic field for radial confinement and hyperbolic electrodes creating an electric quadrupole field. The hyperbolic design of the endcaps, pictured in Figure 2.1, leads to a a potential that can be written as

$$U = \frac{U_0}{2d_{trap}^2}(2z^2 - x^2 - y^2). \tag{2.9}$$

U_0 is defined as the difference between the ring endcap U_r and the two endcaps U_e. The characteristic trap size d_{trap} is defined by:

$$d_{trap}^2 = \frac{1}{2}\left(\frac{\rho_0^2}{2} + z_0^2 \right), \ [2] \tag{2.10}$$

where ρ_0 is the central inner ring radius and z_0 is the endcap distance as indicated by Figure 2.1. The optimal ratio between ρ_0 and z_0 is $\sqrt{2}$, which leads to a maximisation of the effective confinement space.
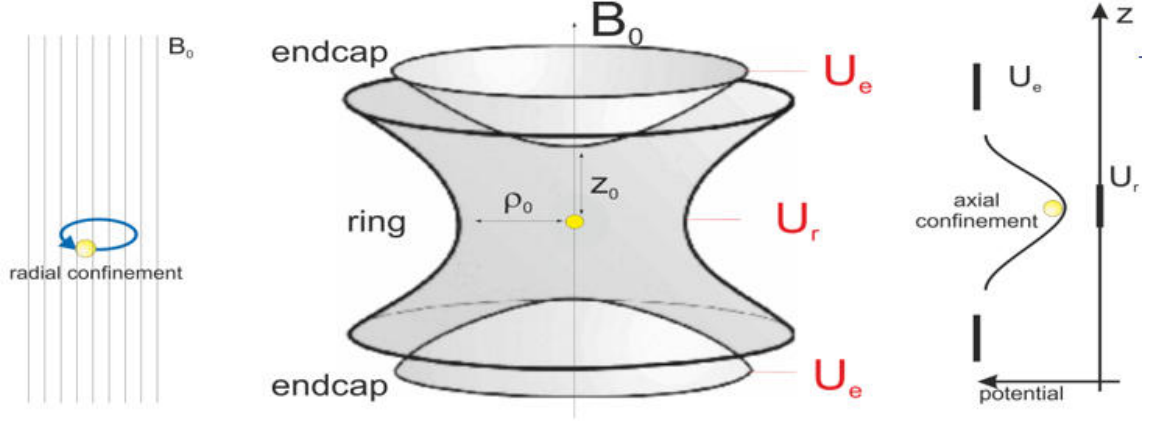
Figure 2.1: Depiction of the electrode design of a hyperbolic Penning trap with the characteristic trap parameters ρ_0 and z_0. The radial confinement is a result of the magnetic field B_0, while the axial confinement is done by the electric potential U_r [2].

2.2.1 Particle Motion in a Penning Trap

It is usefull to look at the axial and the radial motion separately. The axial motion is only dependent on the electric potential and can be described as a harmonic oscillator with the frequency

$$\omega_{\mathrm{z}} = \sqrt{\frac{Uq}{md_{trap}^2}}. \tag{2.11}$$

The radial motion is determined by the magnetic field and the radial component of the electric field. Only considering the magnetic part, the solution would be the so-called cyclotron motion with the corresponding frequency w_c

$$\omega_{\mathrm{c}} = \frac{q}{m}B. \tag{2.12}$$

If one adds the influence of the electric field, the cyclotron motion gets modified to

$$\omega_{\pm} = \frac{\omega_{\mathrm{c}}}{2} \pm \sqrt{\frac{\omega_{\mathrm{c}}^2}{4} - \frac{\omega_{\mathrm{z}}^2}{2}}, \; [2] \tag{2.13}$$

where ω_+ is the perturbed cyclotron motion and ω_- is the magneton, that can be observed in Figure 2.2. This means that the complete ion trajectory and the energy of the ions is just dependent on these three motions, which allows an easy manipulation and detection in the trap. [8]

7

$$\omega_c = \frac{q}{m}B$$

$$\omega_z = \sqrt{\frac{qU}{md^2}}$$

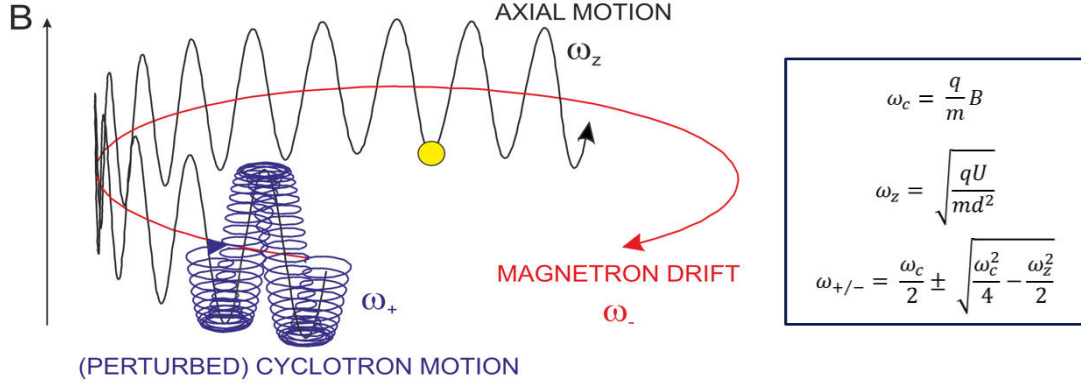$$\omega_{+/-} = \frac{\omega_c}{2} \pm \sqrt{\frac{\omega_c^2}{4} - \frac{\omega_z^2}{2}}$$

Figure 2.2: Motion of a single particle in a Penning trap. The axial motion ω_z is described by a harmonic oscillation caused by the electric quadrupole field. The magnetron motion and the perturbed cyclotron motion can be explained by a combination of the radial electric field component and the magnetic cyclotron motion [2].

2.3 Electron Beam Ion Trap

The Electron Beam Ion Trap (EBIT) is an ion source and an ion trap at once. The possibility to store ions up to ten seconds and release them instantaneously is crucial for the capturing procedure of the Penning trap.

2.3.1 Ionisation Process

The underlying ionisation principle is electron-impact ionisation of atoms trapped in the drift chamber of the EBIT. Electron impact ionisation describes the Coulomb interaction of an accelerated electron with a valence electron of the atom. If the energy transfer to the valence electron is higher than its initial binding energy, the charge state of the atom will increase by one.

$$X^{q+} + e^- \rightarrow X^{(q+1)+} + 2e^-, \tag{2.14}$$
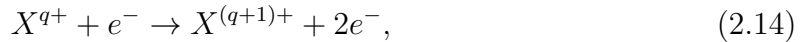
is a simplified depiction of this process. A point of interest is the cross section of this process for a given atomic shell, that can be written as the sum of the cross sections for each electron

$$\sigma_{q+\rightarrow(q+1)+} = \sum_{k=1}^{N} \sigma_{q+\rightarrow(q+1)+,k}, \tag{2.15}$$

with k going form the the quantum number of the lowest possible electron in the shell to the highest state occupied by an electron. With the formula of Lotz, the cross section for

the release of a single electron of the k-shell can be described by the following equation

$$\sigma_{q+\to(q+1)+,k} = \frac{4.5 \cdot 10^{-14} n_k}{E_e I_k} \ln\left(\frac{E_e}{I_k}\right).$$
(2.16)

E_e stands for the energy of the free electron, I_k for the ionisation energy of the bound electron and n_k for the number of electons bound in the shell. [9, 10]

To find the maximum ionisation efficiency it is of the essence to maximize the cross section. The optimal ratio between E_e and I_k can be obtained by maximizing the factor $\ln(E_e/I_k)/(E_e \cdot I_k)$. The resulting ratio can be written as a function of the Euler number e:

$$E_e = \text{e} \cdot I_k \approx 2.7 \cdot I_k.[10]$$
(2.17)

2.3.2 Ion Confinement

To enable the production of highly charged ions, it is necessary to trap already produced low charged ions during the further ionisation process. The confinement technique is comparable to the one used in Penning traps, as it uses a combination of an axial electric field and a magnetic field. In contrast to the "classic" Penning trap, the magnetic field of the EBIT is not the primary reason for the radial confinement. The axial potential is created by drift tube electrodes and can be written as

$$V_{\text{axial}} = -qU_{\text{trap}} = q(U_{\text{ext}} - U_{\text{drift}}),$$
(2.18)

with the trap depth being the difference between first drift tube U_{drift} and the extraction potential of the middle drift tube U_{ext}.
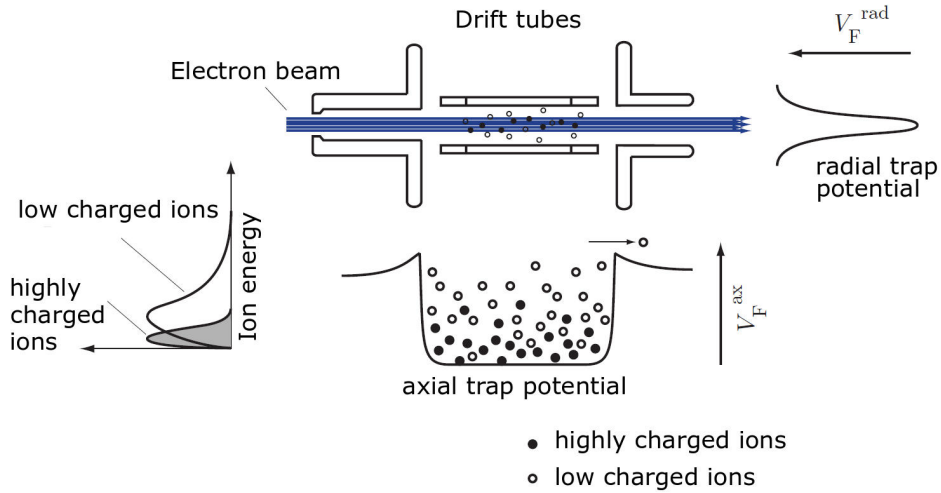

Figure 2.3: Schematic drawing of the axial and radial trap potential inside the drift tube section of the EBIT.[11]

To describe the radial potential of the trap two effects have to be taken into account. The main contribution to the potential is the electric field created by the electron beam. The secondary contribution is the magnetic field applied in axial direction. The magnetic field is needed to focus the electron beam towards the center of the trap, but it also effects the ions. The resulting potential is given by

$$V_{\text{radial}}(r) = V_{\text{e}}(r) + V_{\text{mag}}(r) = qU_{\text{e}}(r) + \frac{qB^2r^2}{8m_{\text{I}}}, [12] \qquad (2.19)$$

with U_{e} being the influence of the space charge of the electron beam. The axial and radial potentials can be seen in Figure 2.3

2.3.3 Wien Filter

A Wien filter is a widely used component used for particle separation and measurement of different particle velocities. Using a magnetic field parallel to the beam direction and an electric field which is perpendicular to the upcoming particle beam is resulting in a force acting on charged particles, that can be described by

$$F_{\perp} = q(E - B_{\parallel}v_z) \qquad (2.20)$$

where $F_{\perp}$ is the force perpendicular to the speed v_z, q stands for the charge of the particle. [13] By means of this expression one can derive the Wien condition for a charged particle to pass the filter as shown in Figure 2.4.

$$v_z = E/B. \qquad (2.21)$$

Using the equation for the particle energy induced by an acceleration voltage $E = qU_{ext}$, one can find a connection between the Wien filter ratio and the mass-over-charge ratio of the outcoming ions

$$E = qU_{\text{ext}} = \frac{1}{2}mv_z^2 \implies \frac{E}{B} = \sqrt{\frac{2q}{m}}. \qquad (2.22)$$

This result shows, that one can select single charge states using a Wien filter provided he knows the atom mass m of the produced ions. Figure 2.4 illustrates this selection.[14]
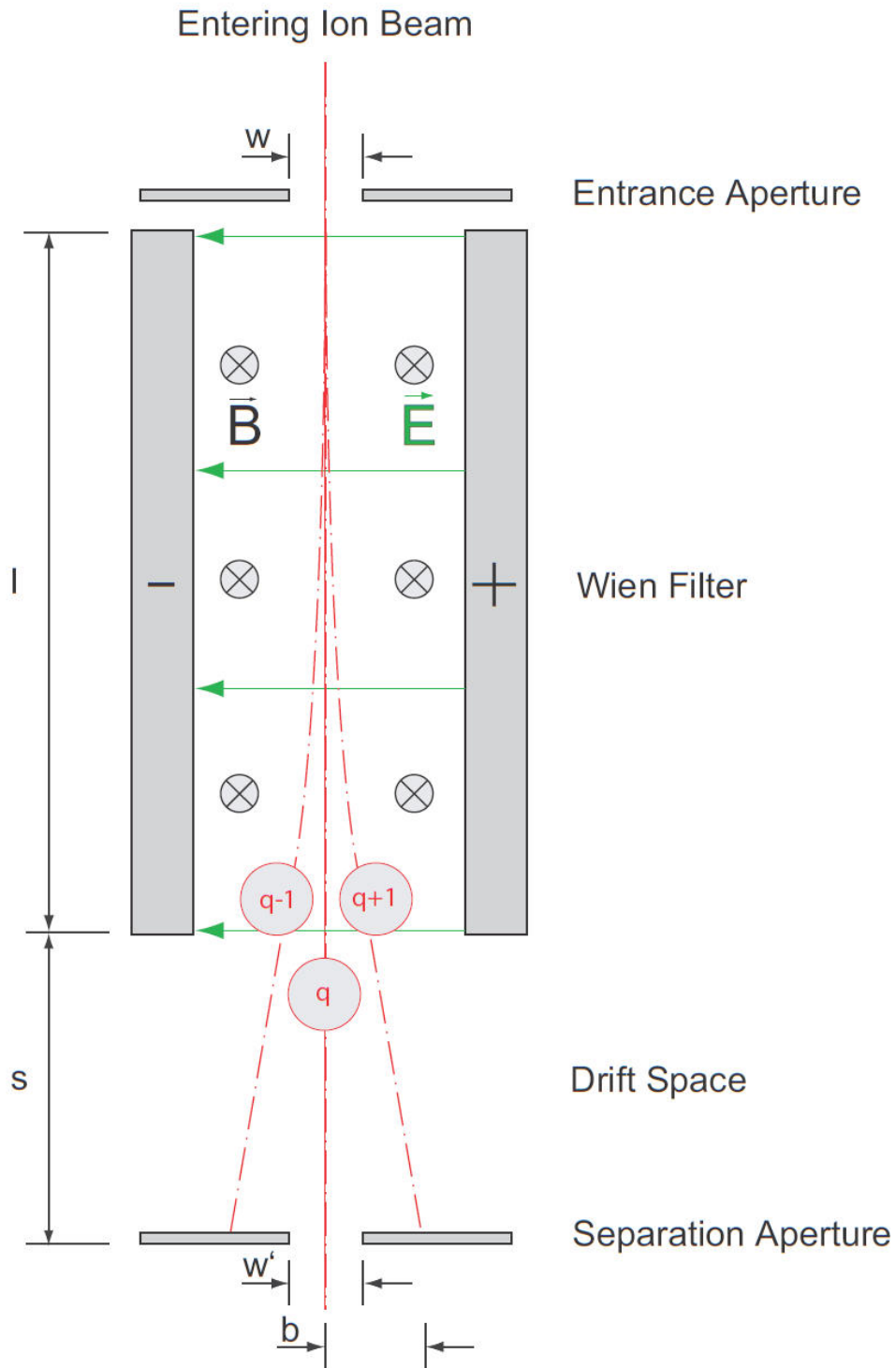
Figure 2.4: A drawing that shows basic principle of a Wien filter. Electric and magnetic fields cause a charge separation of an ion beam inside a Wien filter [15].

3 Experiment Overview

HILITE can be splitted into three different, the ion source, the beam line and the superconducting magnet housing the ion trap. The complete setup can be viewed in Figure 3.1. Since HILITE is designed to be a portable experiment, this separation is not only theoretical but can also be done physically to ensure easy transportation. It is therefore natural to explain all different parts on their own.
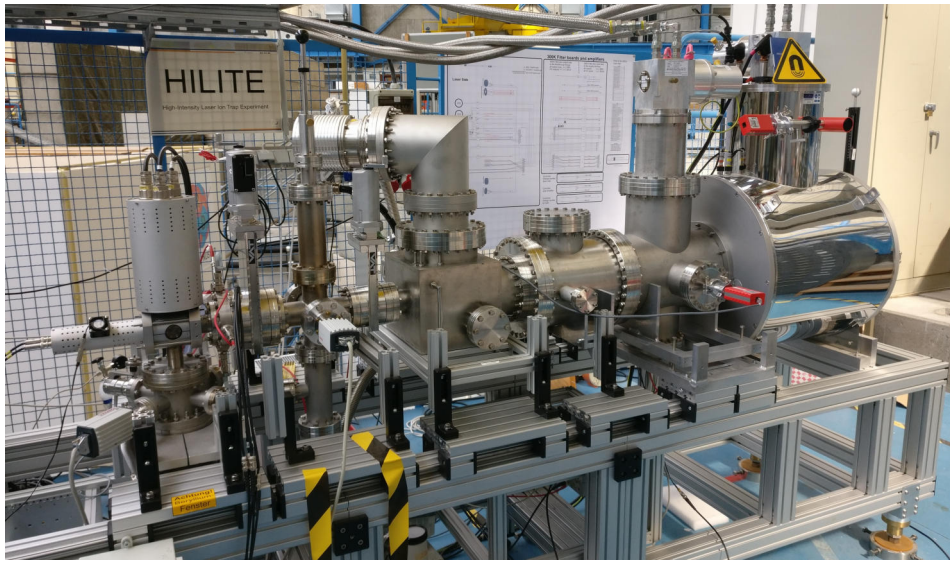
Figure 3.1: A picture of the HILITE setup. EBIT (left), beam line (center) and the magnet (right) are visible.

3.1 Electron Beam Iron Trap

The ion source used in HILITE is a commercial Dresden EBIT, (Electron Beam Ion Trap) based on the work of E.D. Donets [16] that can be viewed in Figure 3.3. In order to provide a clear explanation of the working principle of the EBIT, it is best to distinguish between three different parts in the setup.
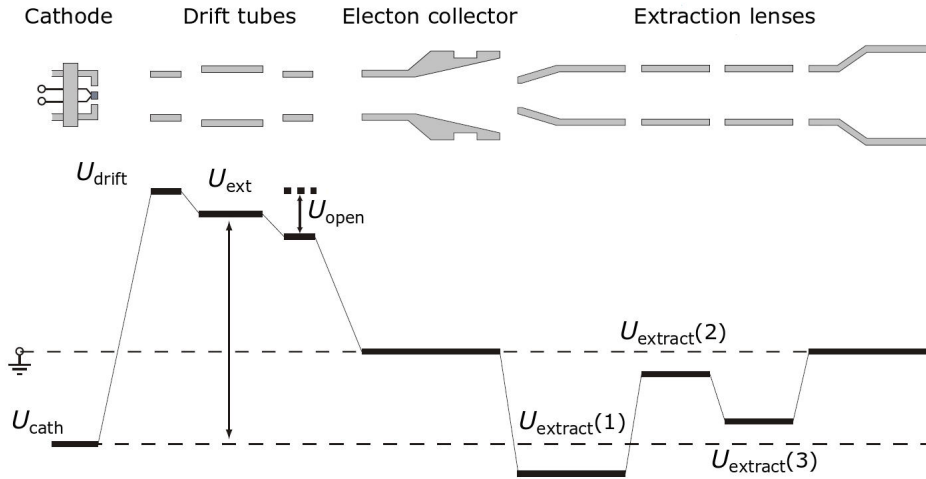
Figure 3.2: A depiction of the electrodes and the created potentials in the EBIT [5].
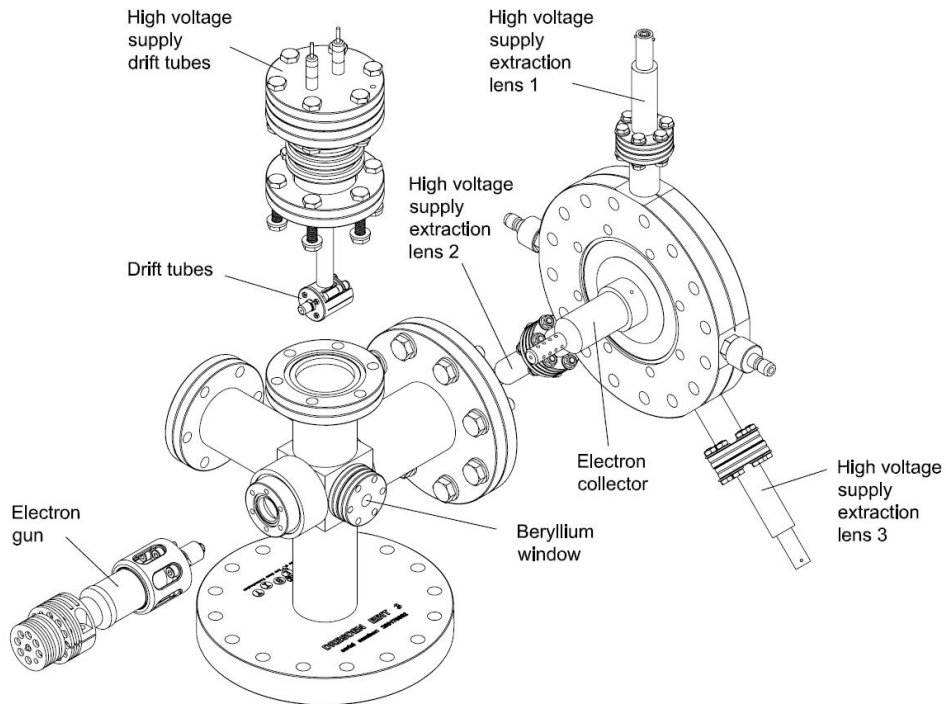

Figure 3.3: A detailed view of the EBIT components with split up electron gun and ion extraction [5].

1. The first part of the EBIT is the cathode section where the electron beam is produced. Free electrons are provided by a built-in iridium cer (IrCe)-cathode and get accelerated by a potential U_{cath} applied by an electrode next to the IrCe-cathode.

13

2. The second part is the ionisation chamber. To focus the electron beam in the center of the chamber a magnetic field is applied by a permanent magnet around the vessel. Inside the chamber is the drift tube which consists of three separate ring electrodes (U_{drift}; U_{ext}; U_{open}). During operation, in the so-called "closed mode", the first and third electrode are set to U_{drift} while the central one is set to ($U_{drift}+U_{trap}$), forming a potential well along the beam axis. The ions produced by electron-impact ionization are now confined until the trap is opened by a change in the potential of the third electrode from U_{drift} to ($U_{drift}+U_{open}$) < ($U_{drift}+U_{trap}$).

3. The third part is the electron deflection and the ion beam focus. This is achieved by three electrodes that are located at the end of the EBIT.

All three parts can be observed in Figure 3.3. Note, that the electron beam gets further accelerated by the drift tube potential, so the resulting electron energy is:

$$E_{\mathrm{e}} = (-U_{\mathrm{cath}} + U_{\mathrm{ext}}) \cdot e. [5] \tag{3.1}$$

3.2 Beam Line

The main purpose of the beam line is the selection and transport of the ions to the trap. In order to achieve sufficient charge state selection, a Wien filter has been implemented right after the EBIT. To focus the ion beam on the Wien filter, and therefore ensure a high ion count rate after the filter, a 4-way deflection was implemented right in front of the Wien filter. Since setting up the system takes a lot of time, only the residual gas has been measured with the Wien filter, as it was crucial to distinguish different peaks. The last important part of the beam line is an einzel lens located between the Wien filter and the Penning trap. The main task of this einzel lens is to focus the beam into the trap and the detection system.

3.3 Ion Trap

Since the classical hyperbolic Penning trap is unwieldy and hard to implement in an experimental setup because of the lack of interacting possibilities with the trapped ions, other solutions needed to be found. This is why modern traps often diverge from the original layout. One of this divergences is the cylindrical open-endcap Penning trap used at HILITE [17, 18].
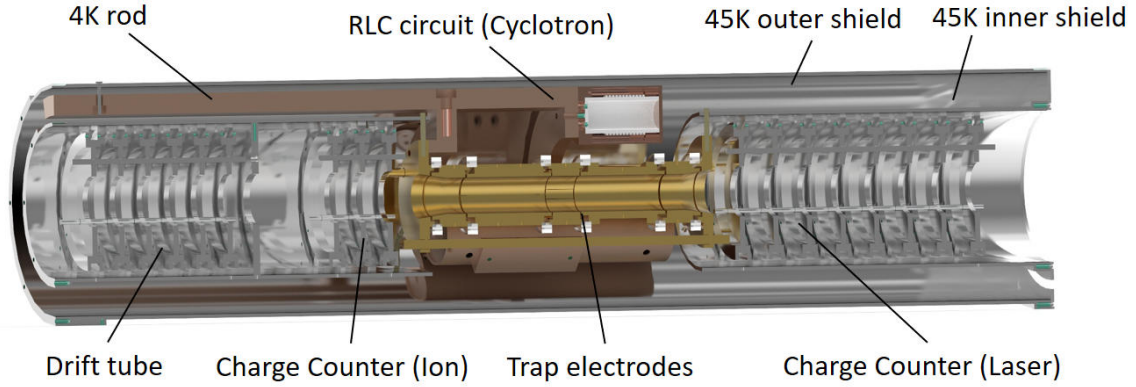
Figure 3.4: A CAD plot of the HILITE trap setup with the surrounding deceleration and detection system.

In contrast to the closed hyperbolical trap, the cylindrical open-endcap Penning trap grants access in beam direction. This is realised by a change in endcap design shown in Figure 3.4. The ring electrode is cylindrical in shape and the endcap electrodes are reduced to two ring electrodes elongated along the z-axis. The elongation is needed to compensate the changes in the quadrupole field close to the trap center. The trap consists of the endcap electrodes, two capture electrodes and an 8-fold segmented ring electrode at the center for cooling and detection. The electrodes are thermally connected by sapphire rings. Outside of the trap are two charge counters used for non-destructive detection. Those charge counters consist of a row of aluminum baffles that measure the image charge induced by bypassing ions.[8] The last crucial part of the trap is the pulsed drift tube that is used for slowing down the ions in front of the trap in order to perform dynamic ion capture. This puled drift tube is set up to discharge in around 30 ns making efficient ion deceleration possible.
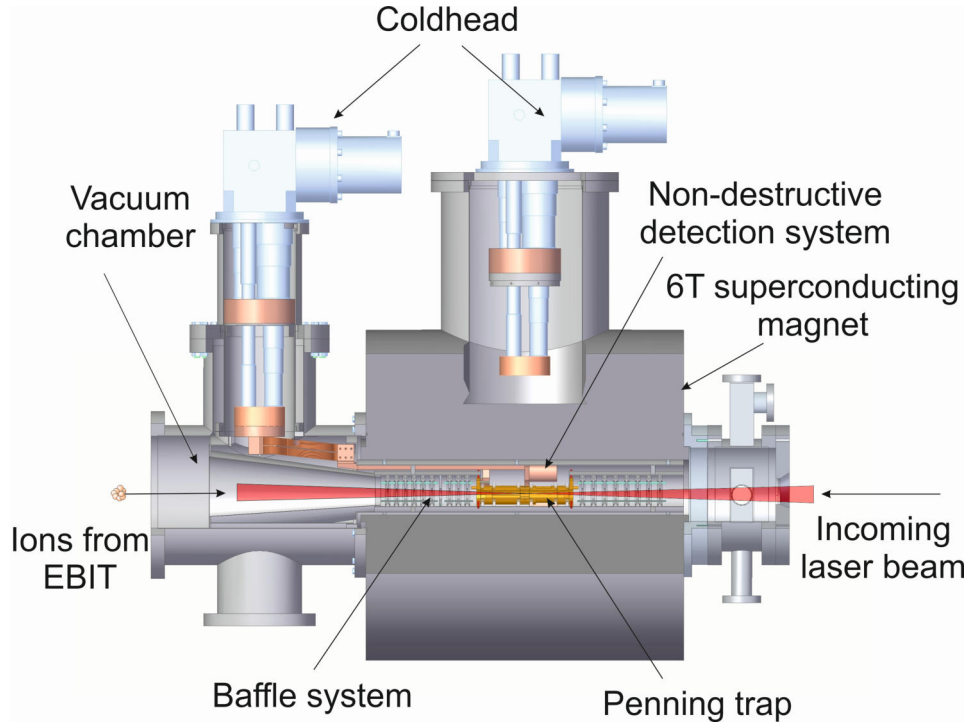
Figure 3.5: The superconducting magnet for the HILITE Penning trap. Indicators show the intended use during a laser experiment.

The structure following around the electrode setup is shown in Figure 3.5 and consists out of the infrastructure for cooling and the magnet system. The magnet used in HILITE is a 6 T superconducting magnet and has another separate cold head and vacuum chamber to ensure stable working conditions. The cooling of the Penning trap is realized by another separate cold head, located on the ion side of the trap. It consists of a two stage cooling system with a 45K stage connected with the thermal shield of the trap and a 4 K second stage connected directly to the trap. A convenient design choice was to locate the cryo-dependent trap electronics on the thermal connection since it saves precious space.

3.4 Measurement Parameters

Since some of the parameters used in the measurement self-explanatory, Table 3.1 provides a short list of all relevant parameters.

Table 3.1: A list of the important parameters for the experimental setup.

Parameter	Usable range	Comment
I_{cath}	1800 to 2400 mA	Electron emission EBIT
U_{cath}	-1000 to -3000 V	Electron acceleration
Breeding time	5 to 10000 ms	Time between EBIT opening pulses
U_{drift}	750 to 3000 V	First drift tube potential
U_{ext}	$U_{\mathrm{drift}} + U_{\mathrm{trap}}$ V	Ion acceleration potential
U_{trap}	0 to -U_{drift} V	EBIT trap depth
U_{open}	U_{trap} to -300 V	Opening pulse potential EBIT
$U_{\mathrm{extract}}(1)$	-4300 V	Electron repeller
$U_{\mathrm{extract}}(2)$	-3100 V	Focusing lens EBIT
$U_{\mathrm{extract}}(3)$	-850 V	Focusing lens EBIT
U_{einzel}	0 to 6000 V	Focus lens after Wien filter
U_{PDT}	0 to U_{ext} V	Pulsed drift tube
$U_{\mathrm{C\text{-}Ion}}$	0 to 400 V	Capture electrode ion side
$U_{\mathrm{C\text{-}Laser}}$	0 to 400 V	Capture electrode laser side
U_{MCP}	200/-2200 V	MCP potential back/front
B	0 to 6 T	Magnetic field
p	200 to 500 nPa	Pressure at the EBIT

4 Measurements

4.1 Time-of-flight Measurements

An essential part of this work are time-of-flight measurements. To study time-of-flight, the time difference between the trap opening pulse of the EBIT and the signal on a micro-channel plate (MCP) was read out using an oscilloscope. In order to measure the influence of the complete experimental setup, the MCP had to be implemented at the very end of the magnet that can be seen in Figure 3.1. The resulting distance d between the EBIT drift tube and the MCP is d=(2.46 ± 0.01) m. On one hand, maximizing the distance increases the time delay between different charge states and ion energies, but on the other hand all the influences in between, like the strong magnetic field have proven to make measurements more challenging.
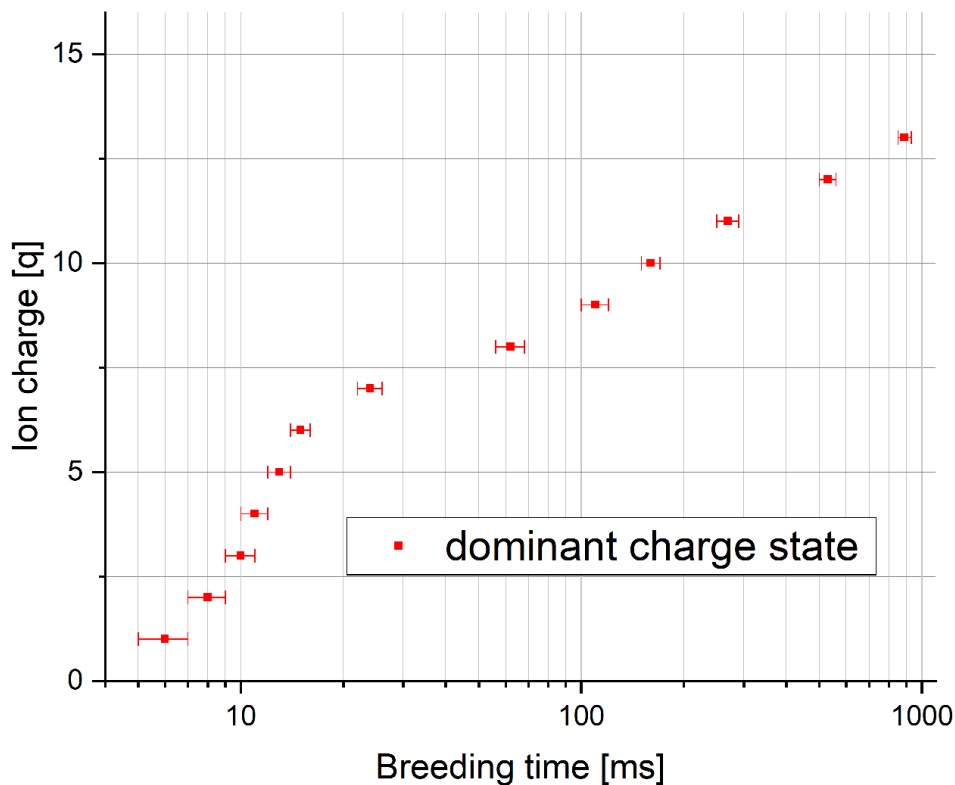

Figure 4.1: The most prominent charge state as a function of the breeding time.

To measure the complete ion spectrum emitted by the EBIT, ion traces have been recorded for different breeding times, since this parameter defines the dominant charge

state as can be observed in Figure 4.1. In order to find the precise peak position, a suitable fitting formula accounting for both, the ion beam spread and the discharge of the MCP, needed to be found. Furthermore, a secondary effect caused by the trap opening sequence of the EBIT induced smaller secondary peaks in the spectrum which can be seen in Figure 4.2(a). To account for that, two Gaussian distributions have been fitted. A primary distribution to measure the peak and a secondary distribution to account for the discharge and the secondary peak. As one can observe, the fit in Figure 4.2(b) shows a good resemblance of the signal in the peak region. It is reasonable to use this kind of process to find data points and estimate error bars.

(a)   (b)
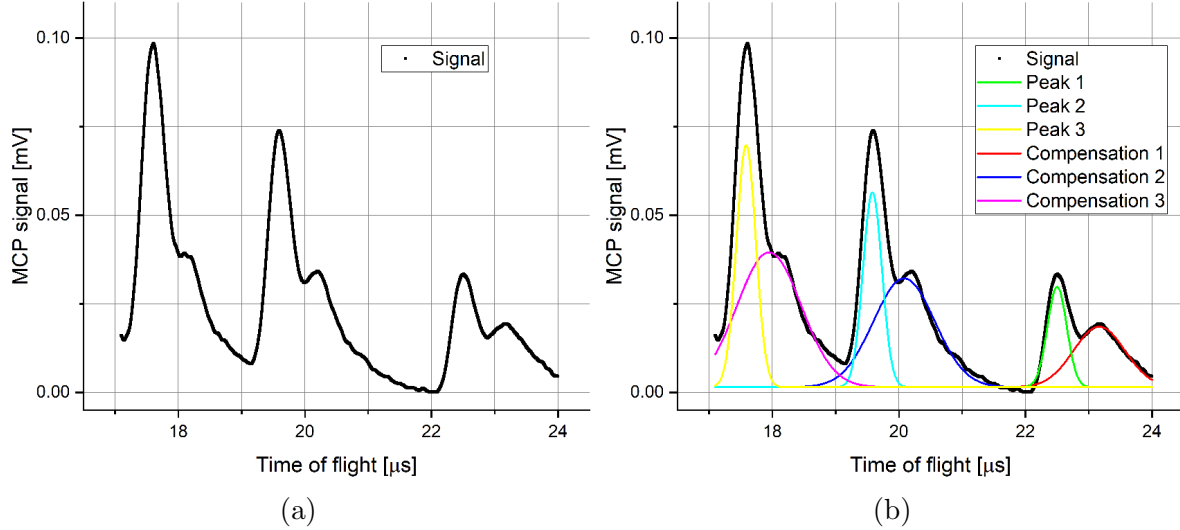
Figure 4.2: (a): The MCP signal of argon ions with a charge of Ar^{3+}, Ar^{4+} and Ar^{5+} with prominent secondary peaks. (b): A Gaussian fit of the argon ions with a secondary compensation function.

The ion energy can be used to connect time-of-flight t to a certain charge state q by

$$E = qU_{\text{ext}} = \frac{1}{2}mv^2 \longrightarrow t = \sqrt{\frac{md^2}{2qU_{\text{ext}}}}. \tag{4.1}$$

By plotting the time against the inverse square root of the charge done in Figure 4.3, the expected linear dependency can be observed.

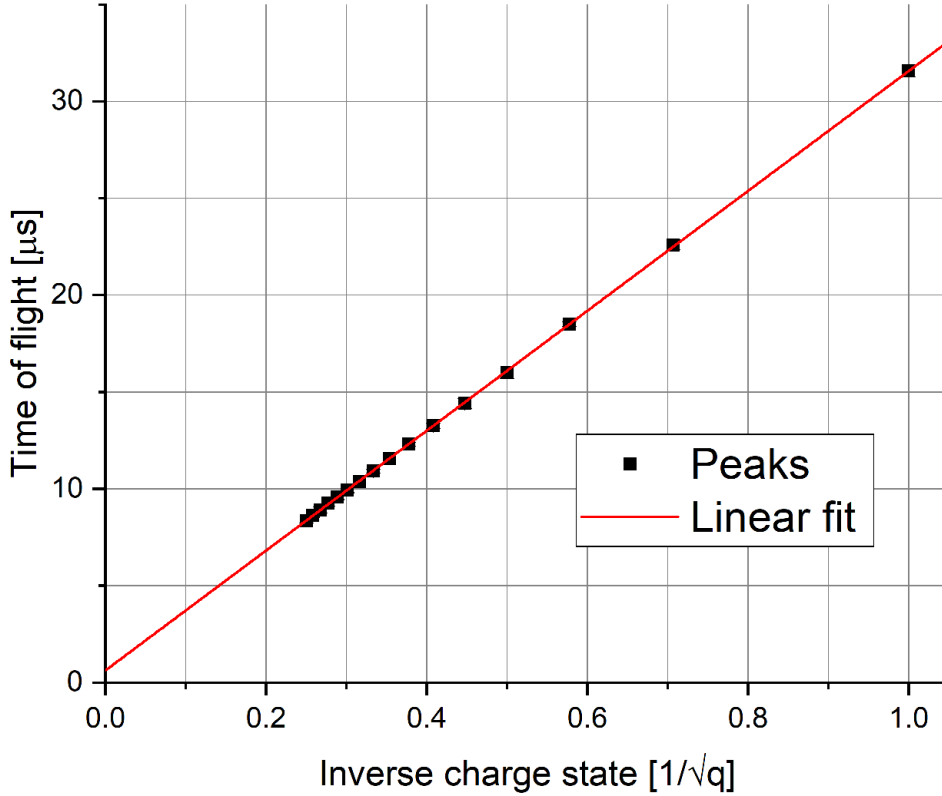Figure 4.3: All charge states that can be obtained by a change in the breeding time are compared in a diagram showing the linear dependency of the ion charge state and the time-of-flight. Error bars are to small to be visualised.

The main readout of the received time-of-flight spectra will be the slope and the y-axis intersection. The slope can be linked to the ion energy as later discussed in subsection 4.2.2. The y-intersection is an indicator for charge-independent delays, caused by electronic imperfections or magnetic/electric fields. For an ideal signal, without external delays, the y-intersection is zero because

$$lim_{q \to \infty}(\frac{1}{\sqrt{q}}) = 0. \tag{4.2}$$

For the current setup, a delay between 500 and 1000 nanoseconds can be measured depending on the the EBIT extraction and the einzel lens focusing.

4.2 Measurements with Argon

Argon is a suitable gas for a variety of reasons. Its easy handling, isotopic purity, low hazard potential and low reactivity make it a widely used gas for testing purposes. In the case of HILITE three other reasons need to be considered:

1. Argon is heavy compared to the anticipated residual gas particles which leads to a low contamination in the ionisation chamber.

2. The ionisation thresholds for argon resemble the energy range of the EBIT with standard operating settings allowing for a broad range of 16 different produced charge states. [5]

4.2.1 Proof of Principle

Before using argon to do systematic time-of-flight measurements one has to make sure that the ions produced in the EBIT are indeed argon ions and one has to determine the different charge states produced in the EBIT. By applying the measurement technique explained in section 4.1, a spectrum of all visible peaks was collected with the following parameter settings shown in Table 4.1.

Table 4.1: A list of the parameters used for the time-of-flight measurement shown in this chapter.

Parameter	Quantity
U_{drift}	1150 V
U_{trap}	60 V
U_{cath}	-3000 V
B	0 T
Einzel lens	0 V

The cascade of peaks was now plotted as a function of the inverse square root of the charge with different starting points as seen in Figure 4.4. Assuming Ar^{1+} for the latest peak results in the closest match with the theoretical prediction as can be seen in Figure 4.4(a). A Ar^{2+} start shown in Figure 4.4(b) diverges from theory. Considering this result, one can verify that the EBIT used in the HILITE experiment can produce all charge states between Ar^{1+} and Ar^{16+}. Using the formula of Lotz one can furthermore understand, that for the given electron energy $(U_{\text{ext}} + U_{\text{cath}}) \cdot e = 4150$ eV and the binding energy of Ar^{17+}: $E(Ar^{17+}) = 4120$ eV the cross section for the ionisation of the k-shell electrons (17+ and 18+) is too small to be seen in the spectrum.[19]
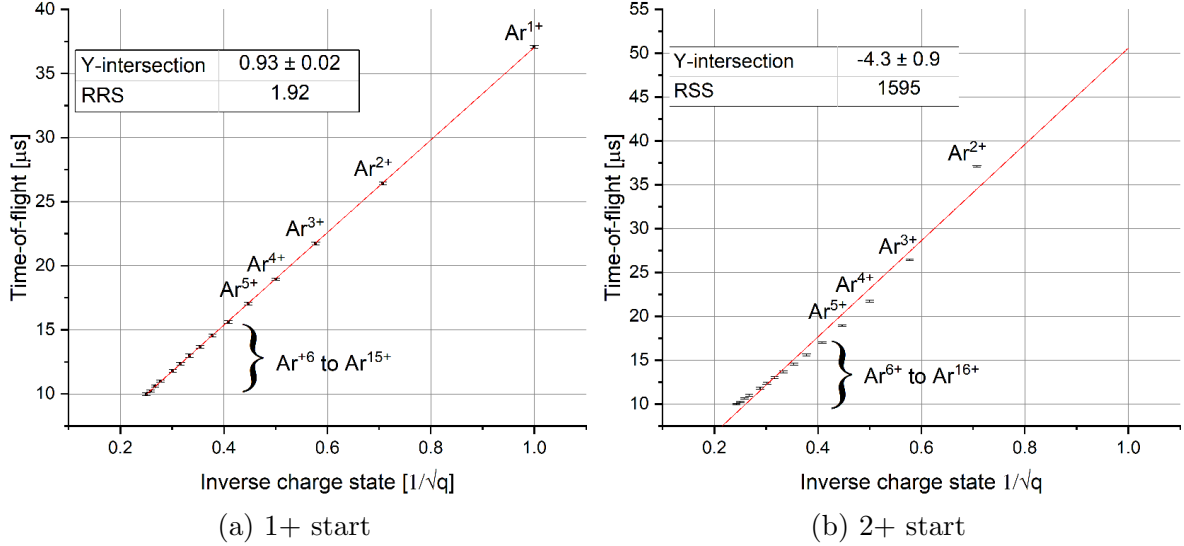
(a) 1+ start

(b) 2+ start

Figure 4.4: The charge cascade of Argon for different starting points. While (a) shows a good resemblance with theory, (b) shows a huge divergence to the fit, that makes Ar^{2+} an non-siutable candidate for later investigations.

Two important parameters, namely the slope and the offset of the charge cascade, can be read out of the fit used in Figure 4.4. The first parameter, the slope can be translated into the ion energy. Using the slope of Figure 4.4 and Equation 4.1 the ion energy per charge E_{Ion}^* can be calculated by

$$E_{Ion}^* = \frac{E_{\text{Ion}}}{q} = \underbrace{\frac{m_{\text{Ar}}d^2}{e}}_{const:=k_{\text{Ar}}} \cdot \frac{1}{a^2}, \tag{4.3}$$

with E_{Ion} being the ion energy, the charge state q, the argon mass m_{Ar}, the distance d, the elementary charge e and the slope a.

The next step is the calculation of the factor k_{Ar} which was found to be

$$k_{\text{Ar}} = \frac{m_{\text{Ar}}d^2}{2e} = \frac{2.46^2 \cdot 39.9623 \cdot u}{2e} = 1.3841 \cdot 10^{-6} \text{ s}^2 \tag{4.4}$$

$$\Delta k_{\text{Ar}} = \Delta d \cdot \frac{2.46 \cdot 39.9623 \cdot u}{e} = 0.0068 \cdot 10^{-6} \text{ s}^2, \tag{4.5}$$

with d beeing 2.46 ± 0.01 m. Using this value one can calculate the energy per charge of the ions depending on the slope of the time-of-flight diagram. By inserting the slope $a = 33.91 \pm 0.05 \ \mu s/\sqrt{eV}$ measured in section 4.1 in Equation 4.3 one can find E_{Ion}^* to be:

$$E_{\text{Ion}}^* = k_{\text{Ar}} \cdot \frac{1}{a^2} = 1098.3 \ \frac{\text{eV}}{\text{q}}. \tag{4.6}$$

The uncertainty of E^*_{Ion} can be estimated by:

$$\Delta E^*_{\mathrm{Ion}} = \Delta a \cdot \frac{2k_{\mathrm{Ar}}}{a^3} + \Delta k_{\mathrm{Ar}} \cdot \frac{1}{a^2} = 7.5 \ \frac{\mathrm{eV}}{\mathrm{q}}. \tag{4.7}$$

The measured energy $E^*_{\mathrm{Ion}} = 1098.3 \pm 7.5$ eV/q needs to be compared to the corresponding extraction potential of the EBIT. The extraction potential of the EBIT U_{ext} is the drift tube potential U_{drift} minus the trap depth U_{trap}. In this case the resulting value of U_{ext}

$$U_{\mathrm{ext}} = U_{\mathrm{drift}} - U_{\mathrm{trap}} = 1090 \pm 4 \ \mathrm{V}. \tag{4.8}$$

The error of U_{ext} is an estimate due to possible inaccuracies of the power supply. To achieve efficient deceleration and further use of the ion beam, the influence of the different parameters has to be investigated.

4.2.2 Ion Energy

For a better understanding of the relation between the acceleration potential U_{drift} and the ion energy per charge E^*_{Ion}, the change in time-of-flight was investigated for different acceleration potentials. The results can be seen in Figure 4.5. Higher energies or ion velocities lead to a shorter time-of-flight and therefore to smaller slopes in the diagram. Using the method explained in section 4.1 the ion energy per charge E^*_{Ion} was calculated using the slope of the time-of-flight-diagrams for $U_{\mathrm{ext}} = 890$ V, 1440 V, 1940 V, 2440 V and 2940 V. A comparison between the measured energy per charge E^*_{ion} and the extraction potential U_{ext} of the EBIT shows the expected linear dependency as can be seen in Table 4.2.

Table 4.2: A comparison of the acceleration voltage U_{ext} and the measured energy per charge. The energy per charge can be calculated using Equation 4.3.

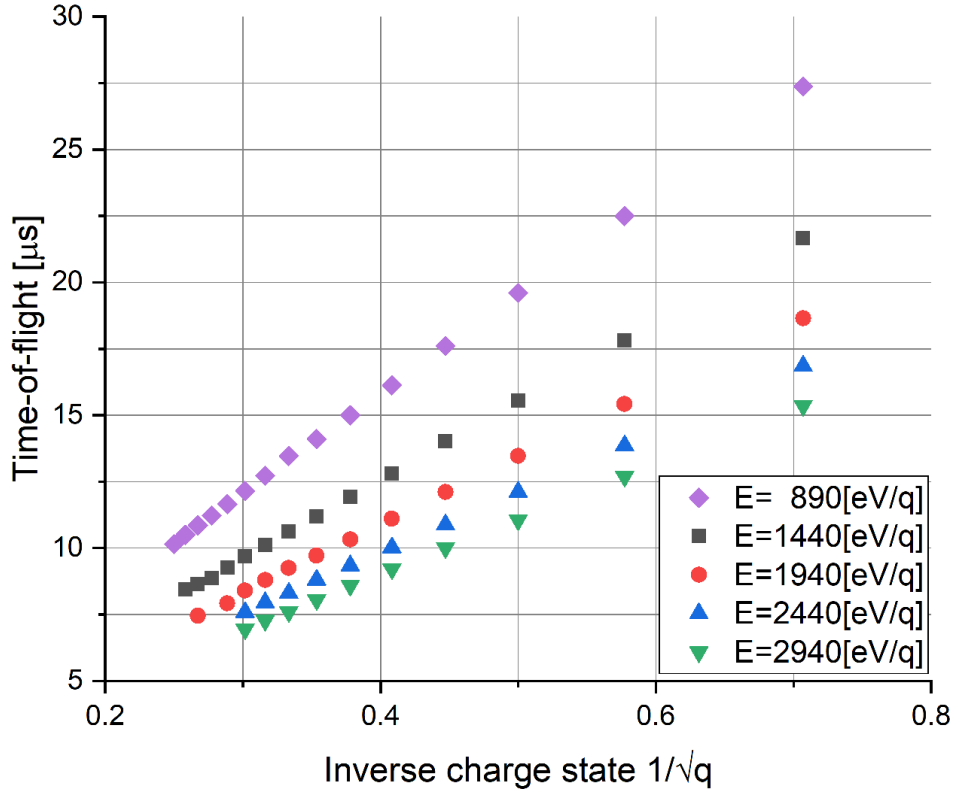| U_{ext} [V]	Slope [μs/$\sqrt{\mathrm{eV}}$]	E^*_{Ion} [eV/q]	$U_{\mathrm{ext}}/ \ E^*_{\mathrm{Ion}}$
890 ± 4	37.64 ± 0.09	891.3 ± 8.4	1.001 ± 0.009
1440 ± 4	29.66 ± 0.06	1436 ± 13	0.997 ± 0.009
1940 ± 4	25.39 ± 0.07	1959 ± 17	1.010 ± 0.009
2440 ± 4	22.78 ± 0.05	2432 ± 23	0.997 ± 0.009
2940 ± 4	20.71 ± 0.08	2943 ± 35	1.001 ± 0.012

Figure 4.5: A comparison of the time-of-flight diagrams for different acceleration voltages between 890 V and 2940 V.

The mean value of the factor connecting U_{ext} and E_{Ion}^* was found to be:

$$\frac{U_{\text{ext}}}{E_{\text{Ion}}^*} = (1.001 \pm 0.010). \tag{4.9}$$

The results show that the ion energy, calculated out of the time-of-flight measurement, is in good agreement with the applied voltage at the EBIT electrodes.
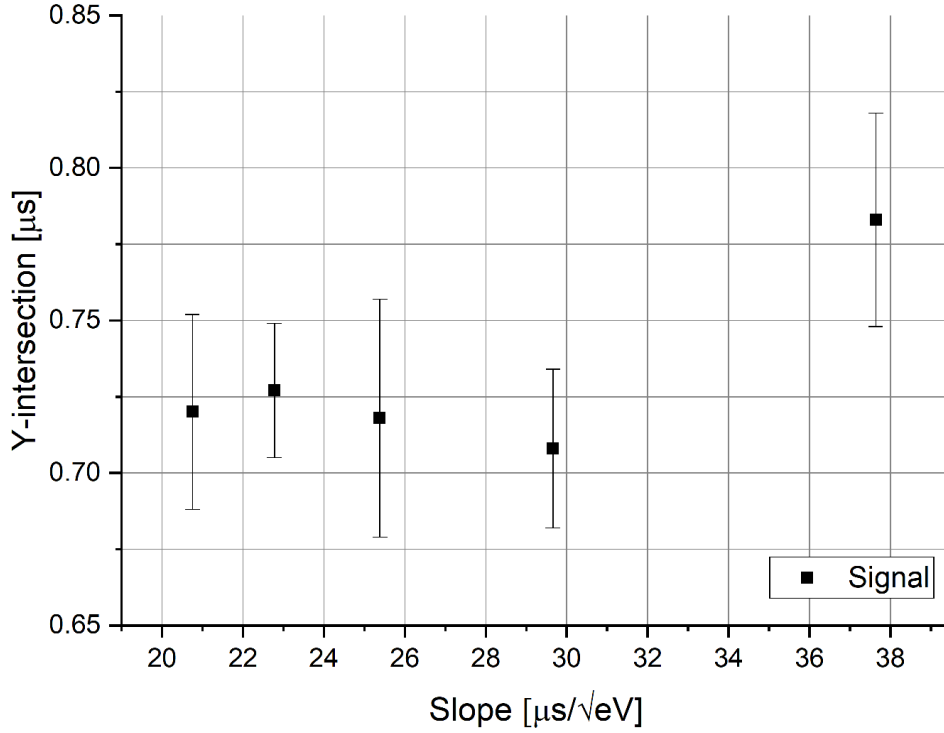
Figure 4.6: A comparison of the y-axis intersection for different acceleration voltages between 890 V and 2940 V.

Another point of interest is the change of the y-intersection. All values are in the expected range of $500 - 1000$ ns discussed in section 4.1, and no energy-dependent change could be found for drift tube energies above 900 V as Figure 4.6 is highlighting.

4.2.3 Signal Delay in a Magnetic Field

An important question is the magnitude of the influence the magnetic field provided by the 6T-superconducting magnet on the time-of-flight of the ions. To evaluate the data, one has to find a theoretical description of the change in time-of-flight related to the magnetic field in the trap. A drawing of the relevant parts is shown in Figure 4.7.
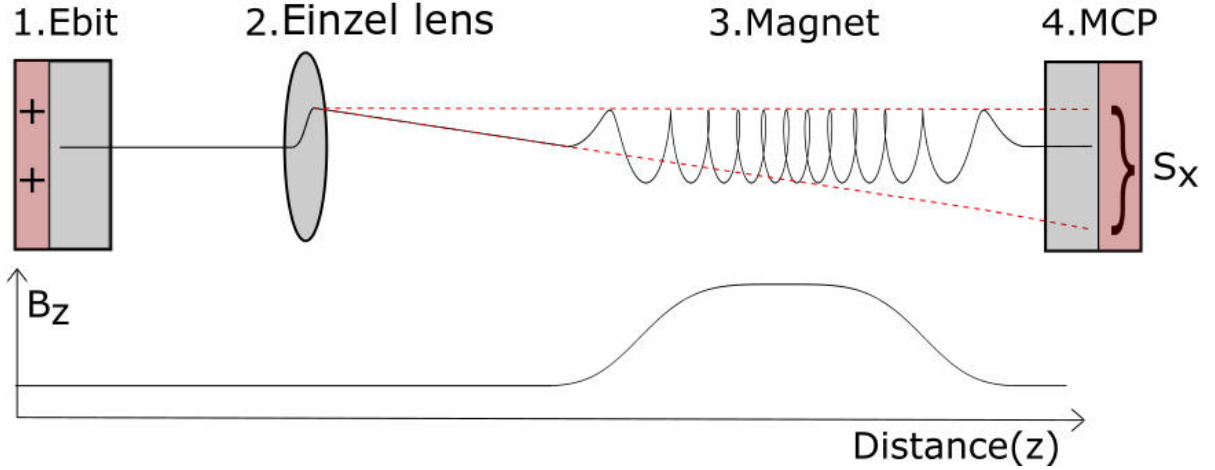
Figure 4.7: A schematic depiction of the ion beam between the EBIT and the MCP. The einzel lens focuses the beam on the MCP giving it an direction perpendicular to the beam. The interaction with the magnetic field causes a circular motion around the z-axis.

1. The ions are accelerated in the EBIT, as discussed earlier in section 2.1. The far field energy of the ions can be approximated by $E = Uq$.

2. The einzel lens focuses the beam leading to a velocity $(v_\perp)$ perpendicular to the magnetic field. The velocity causes the beam to travel the distance S_x perpendicular to the magnetic field. Since the focus point of a electrostatic einzel lens is independent of the charge state, $S_x(q)$ is constant.

3. Due to the Lorentz force the ions perform a circular motion perpendicular to the beam direction and are decelerated dependent on the magnetic field and the initial $v_\perp(0)$.

The charge dependence of the motion in z-direction in front of the lens is given by

$$E = Uq = \frac{1}{2}m_{Ar}v_z^2 \implies v_z = \underbrace{\sqrt{\frac{2U}{m_{Ar}}}}_{const.:=A} \sqrt{q} = A\sqrt{q}. \tag{4.10}$$

The time-of-flight between the einzel lens and the MCP for a given distance S between the einzel lens and the MCP without magnetic field can be written as:

$$t_{0T} = \frac{S}{v} = \frac{S_z}{v_z} = \frac{S}{A\sqrt{q}}. \tag{4.11}$$

Note that S and S_z are interchangeable due to:

$$S_z = \cos(\alpha)S \approx S, \tag{4.12}$$

for small angles α being the angle between the vectors $\vec{S}$ and $\vec{S_z}$.

26

It is useful to introduce some simplifications to the system. Ion beam dispersion will not be considered as it would only slow down the the perpendicular motion in front of the focus point. The magnetic field will be considered homogeneous in z-direction which is only true for complete aligned along the axis of symmetry. However, the effect is small compared to the effect due to the beam angle.

Utilizing the time-of-flight without magnetic field and the distance S_z, one can derive the initial perpendicular velocity $v_\perp(0)$ to be

$$v_\perp(0) = \frac{S_x}{t_{0T}} \implies v_\perp(0) = \underbrace{\frac{AS_x}{S_z}}_{const} \sqrt{q} := A'\sqrt{q}. \tag{4.13}$$

Using the definition of the magnetic moment μ and the fact, that the magnetic field does not work on the ion, one can find a relation for the change of v_z for different magnetic field strengths:[7]

$$\mu_B = \frac{1}{2}\frac{mv_\perp^2}{B}; \quad E_{Ion} = const. \tag{4.14}$$

$$\implies E_{Ion} = \frac{1}{2}mv^2 = \frac{1}{2}m(v_\perp^2 + v_z^2) = \frac{1}{2}m(v_z^2 + \mu_B B). \tag{4.15}$$

Up to a critical field strength B_0, the perpendicular velocity $v_\perp(B)$ can be estimated with the undisturbed motion $v_\perp(0)$. Since μ is an adiabatic constant and will not change apart from a small factor c that is explained in subsection 2.2.1, one can estimate the axial velosity $v_z(B_{max})$ as discussed in section 2.1:

$$\frac{1}{2}mv_z(0)^2 + \mu_{B_0}B_0 = \frac{1}{2}mv_z(B_{max})^2 + c\mu_{B_0}B_{max}. \tag{4.16}$$

With the definition of μ_{B_0} this can be simplified to

$$v_z(0)^2 + v_\perp(0)^2 = v_z(B_{max})^2 + cv_\perp(0)^2\frac{B_{max}}{B_0}, \tag{4.17}$$

which leads to

$$v_z(B_{max}) = v\sqrt{1 - \frac{A'^2c}{A^2B_0}B_{max}}. \tag{4.18}$$

Finally the charge state is connected to the magnetic field-dependent deceleration and one can express the time delay for a distance S_{max} with maximum magnetic field as:

$$t_{delayed} = \frac{S_{max}}{v_z(B_{max})} = \frac{S_{max}}{v\sqrt{1 - \frac{A'^2c}{A^2B_0}B_{max}}}. \tag{4.19}$$

27

For a small factor $\frac{A'^2}{A^2}\frac{c}{B_0}$, a first-order Taylor approximation leads to:

$$t_{\text{delayed}} = t_{0\text{T}} + \underbrace{\frac{t_{0\text{T}} A'^2}{2A^2}\frac{c}{B_0}}_{const.:=P} B_{max} = t_{0\text{T}} + P \cdot B_{max}. \tag{4.20}$$

Using the acquired knowledge, it is possible to perform measurements to determine the constant P connecting the magnetic field and the time delay. As a first step, the charge cascades discussed in section 4.1 have been recorded in steps of 0.5 T. To verify that a change in magnetic field does not influence the slope of the time-of-flight curves, the time delay per tesla P for different charge states was first determined individually for all charge stages between $q = 1$ and $q = 15$. Figure 4.8(a) shows an example for this determination for $q = 5$. By using a linear fit displayed in Figure 4.8(b), the change of P for different q was found to be

$$\Delta P = (-4,54 \pm 3,60) \cdot 10^{-4} \frac{\mu s}{q}. \tag{4.21}$$

This quantity being small compared to the actual value of P means that one can use the time-of-flight diagrams in section 4.1 to determine the offset of the collected data.
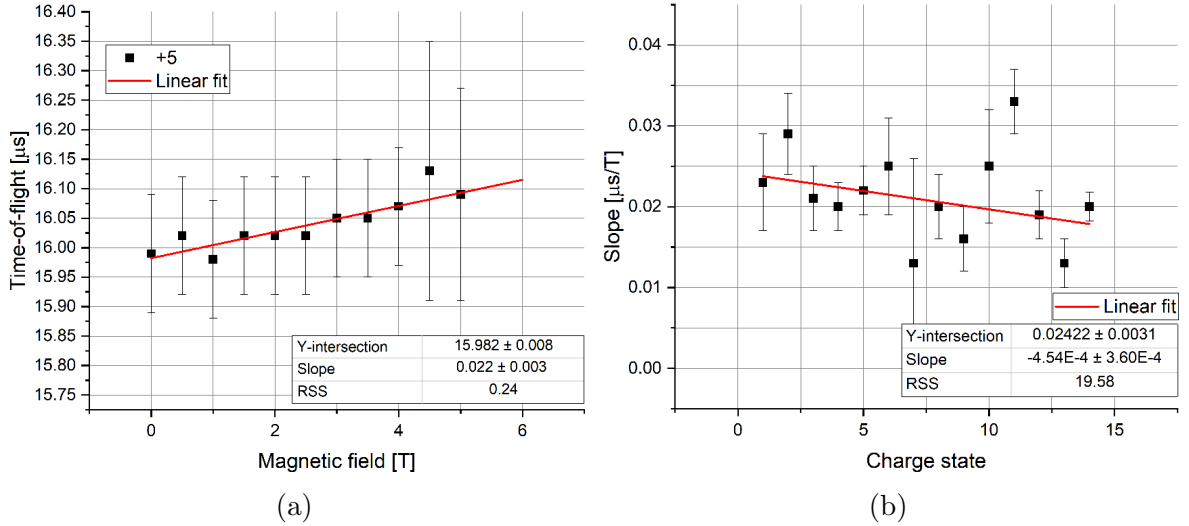

Figure 4.8: (a): shows the change in time-of-flight for a single charge state for different magnetic field strengths. (b): shows a comparison of these changes for the ions Ar^{1+} to Ar^{15+}.

To do so, the average slope of the charge cascades displayed in Figure 4.9(a) was determined and the data points were fitted again with the y-axis intersection being the free parameter as it is shown in Figure 4.9(b) . Since the y-intersection Y_B is directly linked to the charge independent time delay P, Y_B can be written as :

$$Y_{\text{B}} = Y_0 + BP. \tag{4.22}$$

28

Finally this function can be used to determine P with a linear fit shown in Figure 4.9(b) leading to:

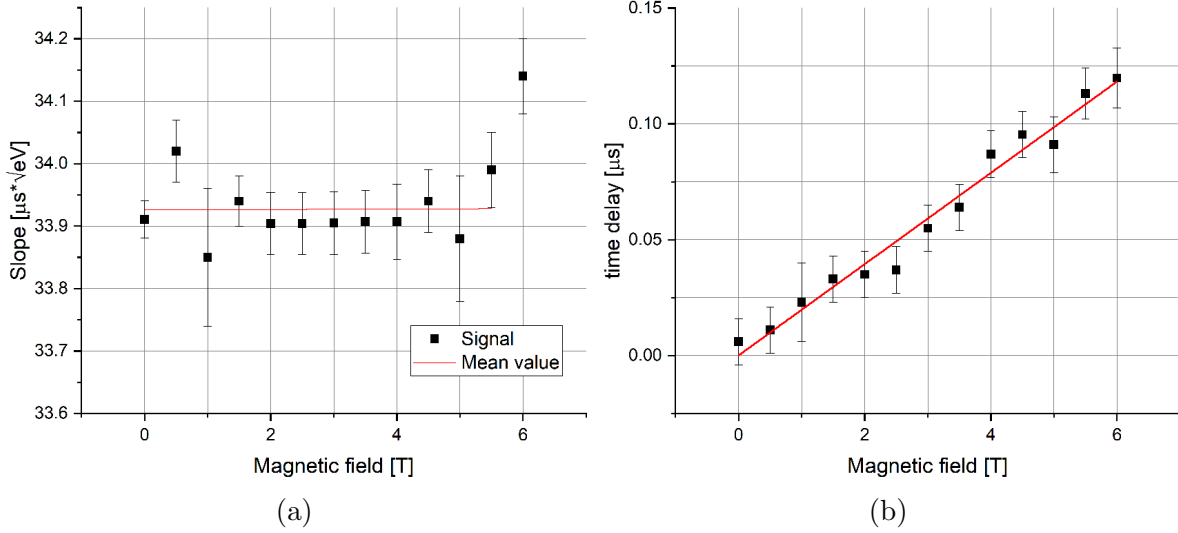$$P = 20 \pm 1 \frac{\text{ns}}{\text{T}}. \tag{4.23}$$

Figure 4.9: (a): shows the slope difference of the time-of-flight diagrams for different magnetic fields. A mean slope was extracted and used in (b): to measure the actual time delay for different magnetic fields.

This value is important in order to receive a proper timing, for the ion deceleration for different magnetic fields. However P describes the total change in time after the magnet, but the deceleration already starts in the magnet, so the delay for the drift tube P_{drift} will be smaller that P.

4.3 Residual Gas

The next chapter will focus the time-of-flight measurements done with the residual gas in the EBIT. In contrast to the previous measurements no external gas source was attached for the actual residual gas measurement. This means, that only the residual gas contributes to the ion count. There are two main reasons to have a closer look on the residual gas:

1. It is a useful diagnostic tool to detect problems with the ion-/electron beam at an early stage. Ions that are not part of expected residual gas spectrum listed in Table 4.3 [20] can provide a hint in the detection of problems in the setup. Extraordinary high count rates of ion species like iron/copper or other metals used in the construction of the EBIT could be explained by a wrong alignment of the electron/ ion beam.

29

2. If one wants to use light ions like carbon or oxygen the resulting ion beam will not only consist of the wanted ion species, but also of other ions comparable in mass. Knowing the residual gas composition can help to identfy those contaminants.

Table 4.3: A list of the atoms and molecules that are expected in the residual gas.[20]

Atom/Molecule	Mass [u]	Partial pressure [Pa]
Hydrogen	1	10^{-10}
Carbon	12	10^{-12}
Nitrogen	14	10^{-11}
Oxygen	16	10^{-12}
OH	17	10^{-12}
H_2O	18	10^{-11}
N_2	28	10^{-11}
CO	28	10^{-11}
CO_2	44	10^{-12}

4.3.1 Measurement Technique

To identify ion species from the residual gas, the measurement had to be performed in two steps: First a calibration measurement followed by a residual gas measurement. The calibration measurement, was done with the same settings as described in Table 4.1 with argon inside at a pressure of $p_{Ar} \approx 5 \cdot 10^{-7}$ Pa. Afterwards the EBIT was evacuated and the time-of-flight of the residual gas ions was recorded for different breeding times at a pressure of $p_0 \approx 2 \cdot 10^{-7}$ Pa. A list of the found peaks and their intensity can be seen in subsection 4.3.4.

4.3.2 Possible Atoms

For a further evaluation, the peaks of the residual gas measurement have to be compared to the argon peaks of the calibration measurement. Since different atoms have different masses, the formula for the time-of-flight is now dependent on two variables: The charge state q and the mass M. Using the time-of-flight plot of argon shown in Figure 4.3 and Equation 4.1, one can extract the y-intersection and an expression connecting the mass-over-charge ration with the time-of-flight of the residual gas peaks t_{res}.

$$t_{Ar} = \sqrt{\frac{m_{Ar}d^2}{2Uq}} + b = \frac{a}{\sqrt{q}} + b \Longrightarrow t_{res} = \frac{a}{\sqrt{m_{Ar}}} \cdot \sqrt{\frac{M}{q}} + b, \tag{4.24}$$

Table 4.4: Shows the quality of alignment of the theoretical and the measured peaks for the different ion species.

Ion species	SSE	COD	Slope (Exp./Theo.)
Oxygen	2.47	0.99981	0.998 ± 0.002
Nitrogen	3.42	0.99966	0.999 ± 0.009
Fluorine	1.04	0.99998	0.999 ± 0.002
Carbon	0.07	0.99998	0.998 ± 0.002

where a represents the slope and b the y-intersection of the argon curve. This equation connects the time-of-flight with the corresponding mass-over-charge ratio.

$$\sqrt{\frac{M}{q}} = \frac{(t_{\text{res}} - b)\sqrt{m_{\text{Ar}}}}{a}.$$

(4.25)

The uncertainty of $\sqrt{\frac{M}{q}}$ can be evaluated using the following expression:

$$\Delta\sqrt{\frac{M}{q}} = \Delta b \cdot \frac{\sqrt{m_{\text{Ar}}}}{a} + \Delta a \cdot \frac{(t_{\text{res}} - b)\sqrt{m_{\text{Ar}}}}{a^2} + \Delta t_{\text{res}} \cdot \frac{\sqrt{m_{\text{Ar}}}}{a}.$$

(4.26)

To identify possible components of the residual gas, the theoretical mass-over-charge configurations of different atoms have to be compared to the measured mass-over-charge ratios found in the residual gas spectrum. A result of such a comparison for oxygen can be observed in Figure 4.10. Using the sum of the squared uncertainties (SSE) and the coefficient of determination (COD) found in Table 4.4 , one can find a way to measure the quality of alignment. In this case a low SSE value and an COD value close to one indicates a good alignment of the data. Especially for elements contained in the air, a huge resemblance could be found, as is listed in Table 4.5. The time-of-flight diagrams for oxygen, nitrogen and carbon/CO_2 can be found in the chapter 7. Even though atomic carbon is not part of the air composition, it is listed here because the peak cascades for carbon and CO_2 are connected. CO_2 is not stable enough to be ionised to more than CO_2^{2+} without loosing its molecular form and is therefore indirectly responsible for the carbon peaks in the residual gas [21].
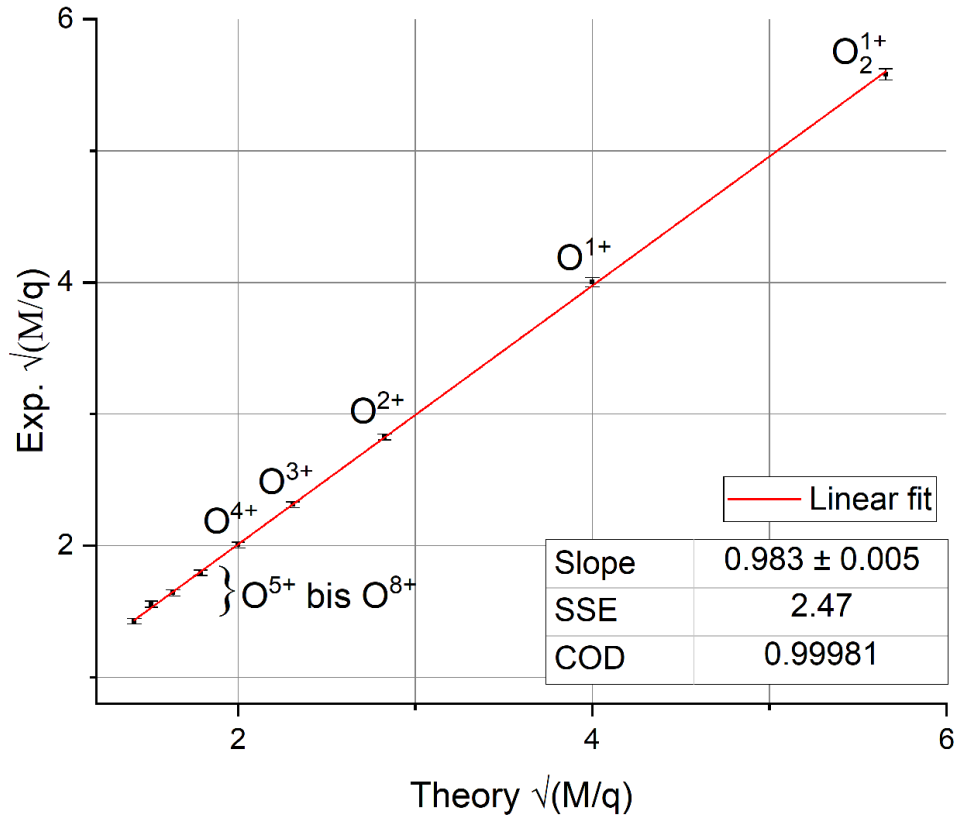
Figure 4.10: A comparison of the theoretical mass-over-charge ratio of oxygen and the corresponding ratio derived from the residual gas peaks. A linear fit is used to determine the quality of alignment.

Besides the group of elements characterized by charge cascades, one could find some ions that are expected to only occur ones or twice in the spectrum. Since non-isotopic hydrogen is the only element with a neutron number of zero, the first peak can be identified as hydrogen quite easily. Helium is another likely candidate, however mass-over-charge ratio from $M/q(\mathrm{He}^+) = 2$ and $M/q(\mathrm{He}^{2+}) = 4$ can not be distinguished from the more prominent oxygen peaks. H_2O can be ionised and a corresponding peak close to the theoretical prediction of H_2O^+ was found. This peak has a very low intensity and can just be a hint at water ionisation.

Equally important to the ions identifiable in the spectrum, is the lack of charge cascades corresponding to Cu, Co and Fe. From this point of view no problem with the alignment of the EBIT is probable.

A list with the mass-over-charge ratios that could be assigned to an atom or molecule is provided in Table 4.5.

4.3.3 Fluorine Determination

An anomaly that needs further investigation are the fluorine-like peaks which have been seen in the residual gas spectrum shown in Figure 4.11. The peaks are part of a charge

cascade that is connected to an atomic mass of $m_I \approx n \cdot 19u$ with $n \in \mathbb{N}$ or are caused by molecules with corresponding mass. If n would be larger than one, more peaks should have been observed in between the fluorine like peaks, which was not the case. Since molecules are not stable for higher charge states because the electron beam dissociates the molecule, it is also unlikely for this cascade to be caused by a single molecule which leaves only two solutions:

1. The peaks are not connected to $m_I \approx 19u$ and therefore are caused by different sources like molecules or isotopes.

2. There is indeed a non-negligible amount of fluorine in the EBIT.

Since there is no fluorine source in the setup, apart from some plastic components, but the plot shows a strong indication of a correlation none of those two hypothesis can be ruled out. A way to verify this would be a measurement of the X-ray spectra emitted by the ions in the EBIT.[22]
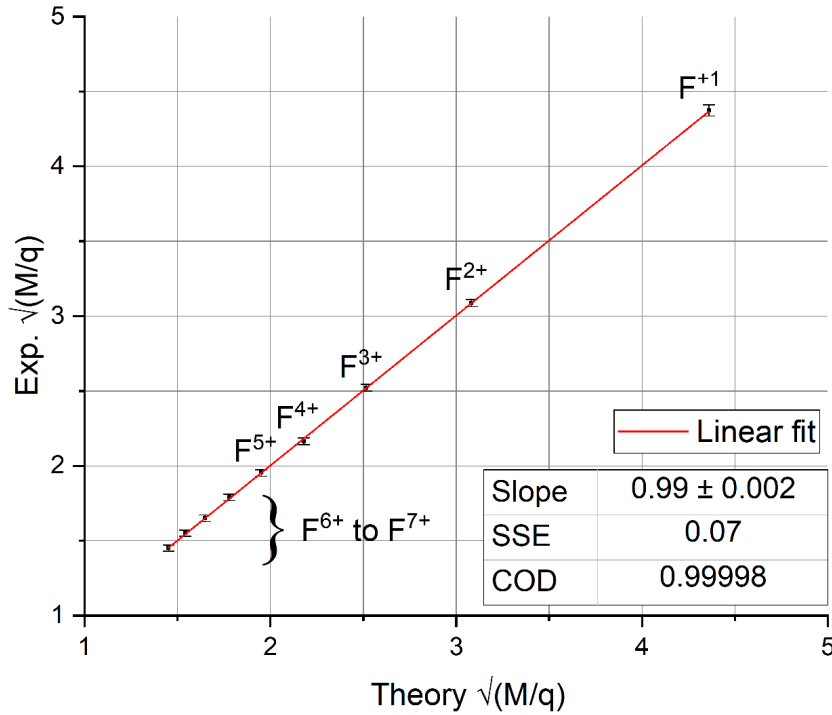

Figure 4.11: A comparison of the theoretical mass-over-charge ratio of fluorine and the corresponding ratio derived from the residual gas peaks. A linear fit is used to determine the quality of alignment.

4.3.4 Summary

Even though the residual gas measurements are largely consistent with similar measurements done at other experiments [20] one should keep in mind that the composition of

Table 4.5: A list of all measured peaks is the residual gas spectrum and their corresponding ions.

ToF [μs]	Mass/charge [$\sqrt{m/q}$]	Corresponding Ions
48.6 ± 0.3	8.34 ± 0.05	Ce^{1+}
38.92 ± 0.3	6.65 ± 0.06	CO_2^{1+}
32.8 ± 0.2	5.58 ± 0.04	O_2^{1+}
31.2 ± 0.17	5.30 ± 0.04	N_2^{1+}; CO^{1+}
27.77 ± 0.15	4.70 ± 0.03	CO_2^{2+}
25.86 ± 0.13	4.37 ± 0.03	F^{1+}
25.18 ± 0.16	4.25 ± 0.03	H_2O^{1+}
23.79 ± 0.17	4.00 ± 0.06	O^{1+}
22.4 ± 0.5	3.76 ± 0.09	N^{1+}
20.72 ± 0.15	3.46 ± 0.03	C^{1+}
18.54 ± 0.1	3.08 ± 0.02	F^{2+}
17.95 ± 0.18	2.98 ± 0.04	-
17.07 ± 0.1	2.82 ± 0.03	O^{2+}
16.03 ± 0.1	2.64 ± 0.02	N^{2+}
14.91 ± 0.1	2.44 ± 0.02	C^{2+}
14.13 ± 0.1	2.31 ± 0.02	O^{3+}
13.42 ± 0.11	2.19 ± 0.02	F^{4+}
13.32 ± 0.15	2.17 ± 0.03	N^{3+}
12.38 ± 0.1	2.01 ± 0.02	O^{4+}; C^{3+}; He^{1+}
12.08 ± 0.1	1.95 ± 0.02	F^{5+}
11.18 ± 0.1	1.79 ± 0.02	O^{5+}; F^{6+}
10.86 ± 0.1	1.74 ± 0.02	C^{5+}
10.3 ± 0.12	1.64 ± 0.02	O^{6+}; N^{5+}; F^{7+}
9.81 ± 0.12	1.56 ± 0.02	O^{7+}; N^{6+}; C^{5+}; F^{8+}
9.07 ± 0.1	1.43 ± 0.02	O^{8+}; N^{7+}; C^{6+}; He^{2+}; F^{9+}
6.59 ± 0.1	0.99 ± 0.02	H^{1+}

the residual gas changes as well, due to different components used in the experimental setup. In addition, an overlap of signals for different ion species with the same q/m ratio cannot be excluded. An X-ray spectroscopy measurement, like the one described in subsection 4.3.3, has to be done in the future to account for that.

Another point is that other changes in atomic mass like the occurrence of isotopes have not been taken into account. Although the two main goals of this measurement stated in section 4.3 could be achieved. An indication for a problem with the electron beam (e.g. misalignment) could not be found and one can now predict the main contaminants for the use of lighter gas targets.

5 Conclusion and Outlook

The main goal of this bachelor thesis was the investigation and characterization of ion bunches extracted from the EBIT and study the influence of the experimental setup on the ions. The applied method of time-of-flight measurements has proven to be a useful tool, leading to the discovery of various ion beam delays, ion charge states and a mass spectrometry of the residual gas.

A variation in acceleration voltage showed, that close to 100% of the drift tube voltage is converted into kinetic energy. Just like the conversion rate, the time offset caused by the EBIT is not dependent on the acceleration voltage in the regime that is likely to be used in the experiment.

The influence of the magnetic field on the time-of-flight was theoretically described and experimentally measured to be $P = 20 \; \frac{\text{ns}}{\text{T}}$.

Finally a mass spectrometry was done with the residual gas in the drift chamber of the EBIT, which led to the determination of oxygen, carbon, nitrogen, hydrogen, helium as well as H_2O and CO_2 as the main components. The mass spectrometry gives an indication of at fluorine presence which should be investigated further.

This information has already been used to find the right parameters for ion capture and has led to a storage time of up to several seconds. This is a huge milestone in the development of HILITE which was partly made possible by this work. The further steps will be the non-destructive detection, cooling and manipulation of ions in the Penning trap.

Even though the main reason for this work was to made this milestone possible, there are other tasks ahead that will profit from this work. An important part of HILITE is the flexibility not only because of the advantage to be transportable, but also in the the preparation of the ion target. In addition, the influence of different magnetic field strengths on charge states can be estimated much easier.

Apart from the immediate use of this thesis for the HILITE project, the scientific work needs to be mentioned. While a lot of those measurement techniques have been done before for different settings, the connection of the charge and the delay in time-of-flight for the beam in high magnetic fields can be useful for a broad range of experiments in different parts of atomic physics and has not yet been examined in this way.

Bibliography

[1] F. M. H. Dehmelt: *Ultrahigh resolution F=0,1 $^3He^+$ Hfs spectra by an ion-storage collision technique.* Phys. Rev. Lett 16,221 (1966).

[2] M. Vogel: *Particle Confinement in Penning Traps.* Springer International Publishing AG (2018).

[3] J. Khuyagbaatar, A. Yakushev, C. E. Düllmann, H. Nitsche, J. Roberto, D. Ackermann, L. Andersson, M. Asai, H. Brand, M. Block *et al.*: *GSI scientific report 2012.* GSI Report **1**, 2013 (2013).

[4] A. Kessler, M. Hornung, S. Keppler, F. Schorcht, M. Hellwing, H. Liebetrau, J. Körner, A. Sävert, M. Siebold, M. Schnepp, J. Hein, and M. C. Kaluza: *16.6J chirped femtosecond laser pulses from a diode-pumped Yb:CaF2 amplifier.* Opt. Lett. **39**, 1333–1336 (2014).

[5] Dreebit: *Instruction Manual Dresden EBIT with Wien Filter* (2010).

[6] W. Nolting: *Grundkurs Theoretische Physik 3.* Springer-lehrbuch (2013).

[7] U. Stroth: *Einführung in die Plasmaphysik.* Skript zur Vorlesung (2007).

[8] A. G. Marshall, C. L. Hendrickson, and G. S. Jackson: *Fourier transform ion cyclotron resonance mass spectrometry.* Encyclopedia of Analytical Chemistry: Applications, Theory and Instrumentation (2006).

[9] G. D. Shirkov and G. Zschornack: *Electron Impact Ion Sources for Charged Heavy Ions.* Springer Science & Business Media (1996).

[10] W. Lotz: *An empirical formula for the electron-impact ionization cross-section.* Zeitschrift für Physik **206**, 205–211 (1967).

[11] F. Ullmann: *Untersuchung der Erzeugung hochgeladener Ionen in einer Raumtemperatur-Elektronenstrahl-Ionenfalle.* Ph.D. thesis, Technische Universität Dresden (2005).

[12] S. I. Molokovski and A. D. Suschkov: *Intensive Elektronen-und Ionenstrahlen: Quellen—Strahlenphysik—Anwendungen.* Springer-Verlag (2013).

[13] W. Wien: *Untersuchungen über die electrische Entladung in verdünnten Gasen.* Annalen der Physik **301**, 440–452 (1898).

[14] N. Hazewindus and J. M. V. Nieuwland: *Wien filter* (1977). US Patent 4,019,989.

[15] Dreebit: *Instruction Manual Wien Filter* (2017).

[16] E. D. Donets: *Historical review of electron beam ion sources.* Review of Scientific Instruments **69**, 614–619 (1998).

[17] G. W. F. Galve, P.Fernandez: *Operation of a planar Penning trap.* Eur. Phys. J.D 40,201 (2016).

[18] P. B. et al.: *Electrons in a cryogenic planar Penning trap and experimental challenges for quantum processing.* Eur. Phys. J. D 40, 201 (2006).

[19] I. Dobrew: *Die Edelgase. Ein kurzer Überblick ueber die Eigenschaften.* GRIN Verlag (2001).

[20] B. Suurmeijer: *Vacuum Science and Technology.* Dutch Vacuum Society NEVAC (2016).

[21] A. Müller and E. Salzborn: *Scaling of cross sections for multiple electron transfer to highly charged ions colliding with atoms and molecules.* Physics Letters A **62**, 391 – 394 (1977).

[22] V. Ovsyannikov and G. Zschornack: *First investigations of a warm electron beam ion trap for the production of highly charged ions.* Review of Scientific Instruments **70**, 2646–2651 (1999).

6 Acknowledgments

A lot of people supported me and helped me to write this thesis. Some helped me with technical problems or with the physics background, some gave me the strength to follow through with my studies and some had their own unique ways to encourage me. However, only two persons managed to combine all that was mentioned above and that is why i want to thank Nils Stallkamp and Tino Morgenroth simply for everything.

Furthermore would like to thank Prof. Dr. Reinhard Dörner for the helpful discussions about magnetism and for providing me with the opportunity to write this thesis, as well as Dr. Wolfgang Quint for believing in me and introducing me to the GSI.

I owe big thanks for everyone working on the HILITE project. Stefan Ringleb who was (together with Nils Stallkamp) the driving force behind the construction of HILITE, for his dedication to taped ions and his many challenging chess games. Markus Kiffer for long fruitful discussions about ions in electric fields. Last but not least Sugam Kumar for his enlightening talk about multi-photon-ionisation, and Manuel Vogel for his enlightening explanations of about everything related to physics.

I would like to explain my gratitude to everybody in the team I worked with. Anahita Khodaparast, Mouwafak Shaaban, Zhexi Guo for their great company and a helping hand whenever i needed one. Kathrin Klaner and Lea Wunderlich for their patience. Davide Racano for his technical expertise and all the other GSI employees for a great work environment.

Since i can not name all the person outside of the world of physics who accompanied me on my way here, i would like to acknowledge everyone equally. But Orwell said that some are more equal than others here we go: I would like to thank Mihaila Stefanova, Jessika Jasiczek and Anneke Pfister who each had their fair share in success. My friends from Frankfurt for the long time we managed to stay together and my sport club the TUS Schwanheim for taking in their "lost son". Andreas Gohlke for his sessions in the last year. I want to thank my father and brother who live way to far from me but never fail to lift me up. And at last i want to thank my mother, for raising me and for giving me an answer to the question what home is.
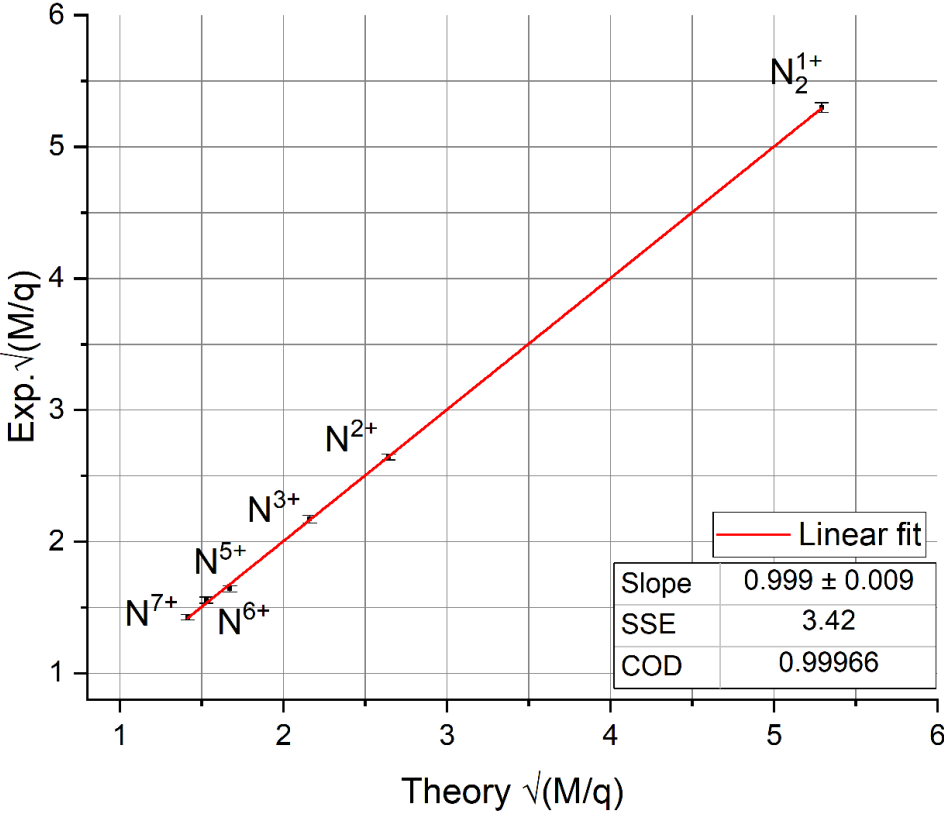
7 Attachments

Figure 7.1: A comparison of the theoretical mass-over-charge ratio of Nitrogen and the corresponding ratio derived from the residual gas peaks. A linear fit is used to determine the quality of alignment.
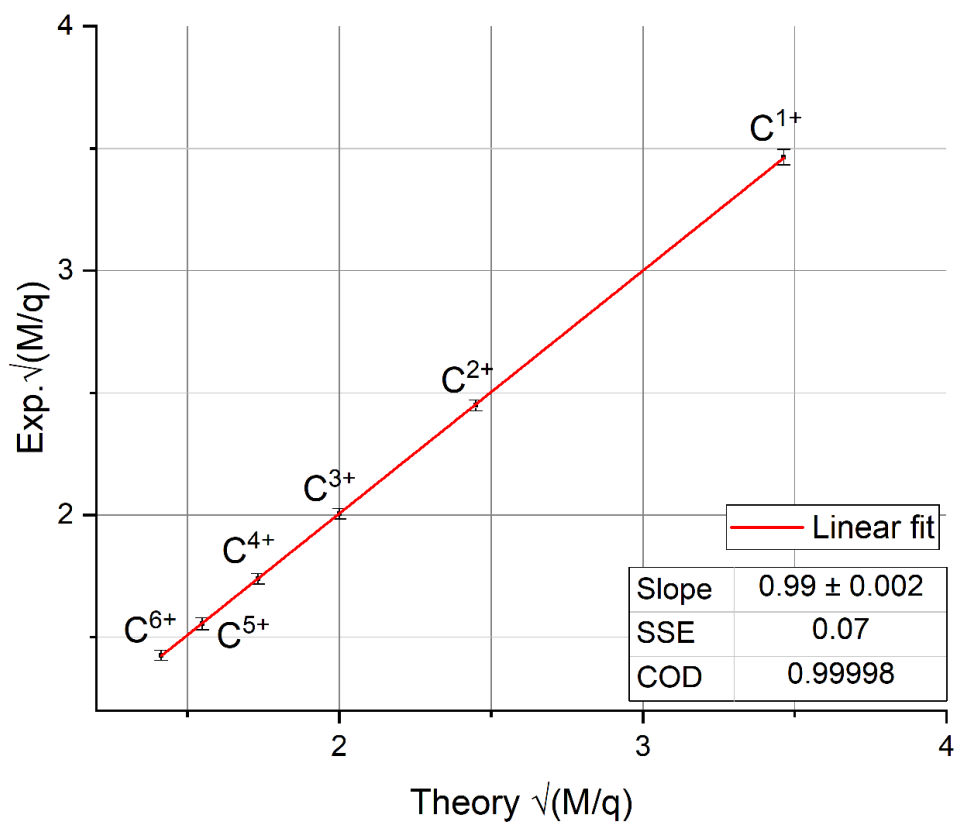
Figure 7.2: A comparison of the theoretical mass-over-charge ratio of carbon and the corresponding ratio derived from the residual gas peaks. A linear fit is used to determine the quality of alignment.